PHOTONICS Research

Indium-doped perovskite-related cesium copper halide scintillator films for high-performance X-ray imaging

Rui Liu,[1] Zhiyong Liu,[1,*] Chengxu Lin,[1] Guangda Niu,[2] Xuning Zhang,[1] Bo Sun,[3] Tielin Shi,[1] and Guanglan Liao[1,4]

[1]State Key Laboratory of Digital Manufacturing Equipment and Technology, Huazhong University of Science and Technology, Wuhan 430074, China
[2]Wuhan National Laboratory for Optoelectronics and School of Optical and Electronic Information, Huazhong University of Science and Technology, Wuhan 430074, China
[3]School of Aerospace Engineering, Huazhong University of Science and Technology, Wuhan 430074, China
[4]e-mail: guanglan.liao@hust.edu.cn
*Corresponding author: zhiyong_liu@hust.edu.cn

Received 29 August 2023; revised 7 November 2023; accepted 14 November 2023; posted 14 November 2023 (Doc. ID 501477); published 1 February 2024

Scintillators are widely utilized in high-energy radiation detection in view of their high light yield and short fluorescence decay time. However, constrained by their current shortcomings, such as complex fabrication procedures, high temperature, and difficulty in the large scale, it is difficult to meet the increasing demand for cost-effective, flexible, and environment-friendly X-ray detection using traditional scintillators. Perovskite-related cesium copper halide scintillators have recently received multitudinous research due to their tunable emission wavelength, high photoluminescence quantum yield (PLQY), and excellent optical properties. Herein, we demonstrated a facile solution-synthesis route for indium-doped all-inorganic cesium copper iodide ($Cs_3Cu_2I_5$) powders and a high scintillation yield flexible film utilizing indium-doped $Cs_3Cu_2I_5$ powders. The large area flexible films achieved a PLQY as high as 90.2% by appropriately adjusting the indium doping concentration, much higher than the undoped one (73.9%). Moreover, benefiting from low self-absorption and high PLQY, the $Cs_3Cu_2I_5$:In films exhibited ultralow detection limit of 56.2 nGy/s, high spatial resolution up to 11.3 lp/mm, and marvelous relative light output with strong stability, facilitating that $Cs_3Cu_2I_5$:In films are excellent candidates for X-ray medical radiography. Our work provides an effective strategy for developing environment-friendly, low-cost, and efficient scintillator films, showing great potential in the application of high-performance X-ray imaging.

https://doi.org/10.1364/PRJ.501477

1. INTRODUCTION

X-ray detection can be divided into direct detection and indirect detection [1–5], and widely used in the fields of medical diagnosis [6,7], safety inspection [8], non-destructive testing [9], aerospace [10], etc. Direct detection has the advantage of high spatial resolution. However, its low attenuation efficiency (α-Se) [11], low stopping power for X-ray energy above 60 keV, and high operating voltage seriously hinder its further applications [12,13]. In indirect X-ray detection, the top scintillator absorbs X-rays to achieve fluorescence conversion while the bottom photodetector array undergoes photoelectric conversion under fluorescence to generate electrical signals, making it a mainstream since it has great stability, high detection efficiency, and low cost [14]. Over the past decades, many scintillators have been commercialized, such as thallium-doped cesium iodide (CsI:Tl) [15,16], cerium-doped lutetium yttrium ortho-silicate (LYSO) [16,17], $Bi_4Ge_3O_{12}$ (BGO) [18], $LaBr_3$:Ce [19], and Tb-doped Gd_2O_2S (GOS) [20]. Despite obtaining significant success, these materials still have boundedness in real applications. They usually involve time-consuming and complex manufacturing processes [21] and require high-temperature and high-vacuum environments [22], which are neither scalable nor environment-friendly. There is an urgent need to explore new scintillator materials with scalable manufacturing processes, high light yields, low cost, and short decay time [23].

Lead halide perovskite materials have been reported as a promising X-ray scintillator due to their simple preparation methods, strong X-ray attenuation ability, and high PLQY

[24,25]. In 2018, the first $CsPbBr_3$ perovskite scintillator device prepared by the thermal injection method was reported, exhibiting a detection limit 420 times lower than typical X-ray medical imaging doses [26]. However, the light yield of $CsPbBr_3$ nanocrystals was only 21,000 photons/MeV [23], much lower than the traditional scintillators such as CsI:Tl (54,000 photons/MeV) [15] and GOS (60,000 photons/MeV) [27]. The severe self-absorption effect caused by the small Stokes shift of $CsPbBr_3$ scintillators leads to low luminescence efficiency [23]. The stability of lead halide perovskite is also a great challenge for practical applications [28]. Thus, researchers tried to replace lead with low toxicity or toxicity-free elements to prepare a series of lead-free metal halide scintillator materials to overcome these problems [29–32].

Among them, inorganic cuprous halide perovskite-related compounds have been extensively studied [33,34] and bloomed into a great deal of optoelectronic devices [35,36]. $Cs_3Cu_2I_5$ is widely used in X-ray detection due to its high luminous efficiency and good stability [13]. The $Cs_3Cu_2I_5$ single crystals fabricated by the Bridgman method showed a light yield of 32,000 photons/MeV [37], and the $Cs_3Cu_2I_5$ films made of ball-milled powders realized the X-ray imaging spatial resolution of 6.8 lp/mm [38]. Researchers continuously explore higher light yield and resolution of $Cs_3Cu_2I_5$ to meet the long-term application in X-ray imaging [39]. Metal ion doping provides an efficacious way to improve the scintillation performance of $Cs_3Cu_2I_5$ [40,41]. Qu *et al.* prepared $Cs_3Cu_2I_5$:Zn nanocrystals by hot-injection with a detection limit of 310 nGy/s and spatial resolution up to 15.7 lp/mm [42], while the material yield of the hot-injection-based nanocrystal fabrication process was low and the energy consumption of the vacuum evaporation procedures was relatively high. Wang *et al.* reported the In^+ doped $Cs_3Cu_2I_5$ single crystals by the vertical Bridgman method showing a high light yield of 53,000 photons/MeV and a low detection limit of 96.2 nGy/s [43]. However, the synthesis of single crystals also requires high cost and complex procedures. Meanwhile, some researchers doped Tl^+ into $Cs_3Cu_2I_5$ to improve its scintillation yields [40,44]. But Tl^+ doping will significantly lead to a very long scintillation decay time, and the doping of highly toxic Tl elements is undesirable [43]. A more efficacious way to prepare $Cs_3Cu_2I_5$ with excellent scintillation yield, high spatial resolution X-ray imaging, simple fabrication procedures, and low cost is needed.

In this work, we demonstrated a facile solution-synthesis route for In^+-doped $Cs_3Cu_2I_5$ powders, which were mixed after grinding completely with PDMS at a ratio of 45% to obtain a flexible film with arbitrary sizes by spin-coating. Appropriately adjusting the indium-doped concentration could significantly improve the PLQY of the $Cs_3Cu_2I_5$ films from 73.9% to 90.2%. Profiting from the high PLQY and ultralow self-absorption, the indium doped $Cs_3Cu_2I_5$ films obtained a high relative light output, more than five times higher than that of the BGO. The $Cs_3Cu_2I_5$:In films exhibited an ultralow detection limit with the doses of 56.2 nGy/s, approximately 98 times lower than the dose of the typical X-ray medical imaging. A high resolution of 11.3 lp/mm was achieved, facilitating $Cs_3Cu_2I_5$:In films to be excellent candidates for X-ray medical radiography. Moreover, our $Cs_3Cu_2I_5$:In films exhibited excellent radiation stability, cycle stability, and water tolerance, enabling high-resolution imaging in various complicated environments.

2. EXPERIMENT

A. Materials

Cesium iodide (CsI, 99.9%), copper iodide (CuI, 99.95%), indium iodide (InI, 99.99%), dimethyl sulfoxide (DMSO, AR), isopropanol (IPA, AR), and polydimethylsiloxane (PDMS) were purchased from Aladdin. All chemicals were used as received without further purification.

B. Preparation of $Cs_3Cu_2I_5$:In Powders and Flexible Films

In a typical synthesis of $Cs_3Cu_2I_5$:0.4%In powders, 2494.2 mg CsI, 1218.8 mg CuI, 3.1 mg InI, and 4 mL DMSO were added to a 10 mL bottle. The mixture was stirred at 75°C for 2 h to fully dissolve the powders. The precursor solution was mixed 1:1 with isopropanol and vigorously vibrated to completely dissolve them. After that, the solution was centrifuged at 9500 r/min for 5 min and the supernatant was discarded to obtain $Cs_3Cu_2I_5$ powders. Wash the $Cs_3Cu_2I_5$ powders three times with isopropanol to remove remains on the surface. Indium-doped $Cs_3Cu_2I_5$-PDMS flexible films were prepared by a simple spin-coating method. The prepared $Cs_3Cu_2I_5$ powders were hand-grinding in an agate mortar to obtain uniform size distribution powders. The PDMS was prepared by mixing two components of Sylgard 184 at a volume ratio of 10:1 and stirred vigorously to mix evenly. After that, the $Cs_3Cu_2I_5$ powders were added at a mass ratio of 45%, and the mixture was stirred for 2 h to disperse completely. A little mixture was sucked, quickly dripped onto the glass slide, and then cured for 1 h at 140°C to form the $Cs_3Cu_2I_5$-PDMS flexible film. The thickness of the films can be easily controlled by adjusting the spin-coating speed from 100 to 800 r/min.

C. Characterization Methods

The crystallinity characterization of the $Cs_3Cu_2I_5$ was analyzed by PANalytical BV X-ray diffraction (XRD). The morphologies of $Cs_3Cu_2I_5$ powders were analyzed by scanning electron microscopy (SEM) on a Nova NanoSEM 450. The X-ray photon spectroscopy (XPS) profile was measured by AXIS-ULTRA DLD-600W. PL and photoluminescence excitation (PLE) spectra were collected on a fluorescence spectrofluorometer (QuantaMaster 8000). The time-resolved PL (TRPL) spectra and PLQY were measured by the fluorescence spectrofluorometer with an integrating sphere. The excitation wavelength was set at 311 nm. The radioluminescence (RL) spectra were taken by a spectrometer (HORIBA FluoroMax-4/Plus) equipped with a photomultiplier tube (PMT, Hamamastu R928P) and an X-ray tube (tungsten target, HORIBA FluoroMax-4/Plus). The detection slit was set at 3 nm, and the X-ray outlet was set to 9 cm away from the samples for all spectral measurements. The X-ray doses were controlled by adjusting the input voltage and current values. A high sensitivity X-ray ion chamber dosimeter (Radcal Accu-Gold+) was used for calibration. To ensure no radiation leakage, all tests were conducted in a lead cabinet shielded from radiation.

3. RESULTS AND DISCUSSION

A. Preparation and Characterization Details of $Cs_3Cu_2I_5$:In Powders

$Cs_3Cu_2I_5$ consists of zero-dimensional electronic structures. According to previous theoretical calculations, Cu 3d orbitals dominantly contribute to the valence band maximum (VBM), while the conduction band minimum (CBM) is mainly composed of Cu 4s and I 5p orbitals [45]. Therefore, exciton transition in $Cs_3Cu_2I_5$ occurs mainly in the Cu-I structures. The substitution of Cu^+ or I^- ions has become the main strategy for modulating the electronic structure and optical properties of $Cs_3Cu_2I_5$. Considering the ionic radius and spatial configuration of Cu^+, In^+ was proved to be an excellent dopant [43]. In this work, we introduce an additional exciton recombination center in $Cs_3Cu_2I_5$ by doping In^+ to improve RL efficiency. The phase purity of undoped and In-doped $Cs_3Cu_2I_5$ powders was measured by XRD. The prepared $Cs_3Cu_2I_5$ powders matched the standard diffractions (PDF#79-0333) exactly, without the existence of impurities [Fig. 1(a)]. With the increase of In^+ doping concentration, the XRD peaks shifted continuously toward the higher values of 2θ. Compared with the undoped $Cs_3Cu_2I_5$, the strongest diffraction peak of $Cs_3Cu_2I_5$:2%In shifted from 26.341 to 26.459 deg implied that In^+ doping decreased the interplanar spacing. Figure 1(b)

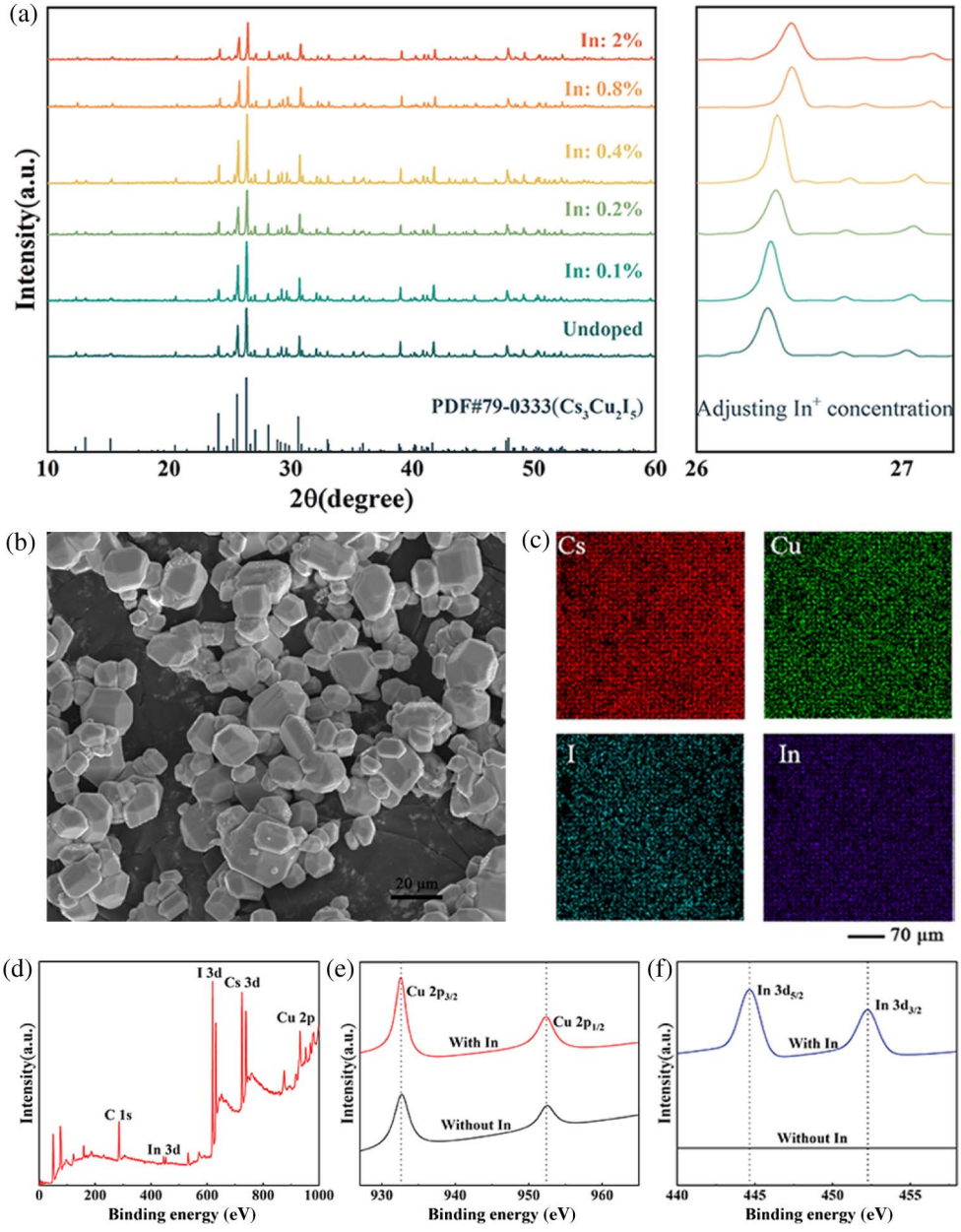

Fig. 1. Characterization details of the $Cs_3Cu_2I_5$:In powders. (a) XRD patterns of the $Cs_3Cu_2I_5$ powders samples doped with different indium concentrations (top), compared with the orthorhombic $Cs_3Cu_2I_5$ at the bottom (PDF#79-0333). (b) SEM image of the $Cs_3Cu_2I_5$:In powders. (c) Elemental mapping images of the $Cs_3Cu_2I_5$:2%In powders. (d) XPS survey spectrum of the $Cs_3Cu_2I_5$:In powders. (e), (f) High-resolution XPS profiles of Cu ($2p_{3/2}$ and $2p_{1/2}$) and In ($3d_{5/2}$ and $3d_{3/2}$) of the $Cs_3Cu_2I_5$ powders synthesized with and without In, respectively.

shows the morphology of the $Cs_3Cu_2I_5$:In powders, an irregular micrometer spherical shape with an average size of 4.16 μm.

The energy dispersive spectroscopy (EDS) and elemental mapping images of the $Cs_3Cu_2I_5$:2%In powders are shown in Fig. 1(c), respectively, confirming that the proportions of Cs, Cu, and I atoms were 32.45%, 17.93%, and 48.15%, respectively, close to the stoichiometric ratio (3:2:5). The In^+ dopant was also detected at 1.47%. To further determine the composition and chemical state of the elements, we conducted XPS on the $Cs_3Cu_2I_5$:In powders, showing peaks of the constituting elements C 1s, In 3d, Cs 3d, Cu 2p, and I 3d [Fig. 1(d)]. The valence state of Cu ions in the $Cs_3Cu_2I_5$:In powders was analyzed in Fig. 1(e). The two peaks located at 932.5 and 952.3 eV were characteristic peaks of Cu^+ $2p_{3/2}$ and Cu^+ $2p_{1/2}$. Moreover, no characteristic satellite peak of Cu^{2+} was observed (approximately 943 eV), further ruling out the presence of Cu^{2+} in the $Cs_3Cu_2I_5$ powders. Two additional peaks in the InI-doped $Cs_3Cu_2I_5$ powders appearing at 444.7 and 452.3 eV attributed to the In 3d further confirmed that In^+ was doped into the $Cs_3Cu_2I_5$ powders [Fig. 1(f)]. These results provided further support for the successful synthesis of the $Cs_3Cu_2I_5$:In powders.

B. Ultraviolet Detection Performance of $Cs_3Cu_2I_5$:In Films

Figure 2(a) shows the optical properties of $Cs_3Cu_2I_5$:In films. The PLE spectrum of the films showed an excitation peak at 311 nm, while the PL spectrum exhibited strong blue emission at 438 nm with a full-width at half-maximum (FWHM) of 84 nm and a Stokes shift of 127 nm. There was almost no spectral overlap between the PLE and PL spectra, indicating that the prepared $Cs_3Cu_2I_5$ materials exhibited ultralow self-absorption [46], which was an indispensable parameter for high-performance scintillators. The PL spectral peaks measured at different doping concentrations showed the same shape but different intensities, indicating that the observed blue emission was caused by radiation recombination in the same excited state [Fig. 2(b)]. As shown in Fig. 2(c), after immersion in deionized water for 1 h, the PL intensity of the films only suffered a slight decay.

The corresponding TRPL decay curves of the doped and undoped films were measured in Fig. 2(d). The PL lifetime of the $Cs_3Cu_2I_5$:In films was 0.9 μs, longer than that of the undoped $Cs_3Cu_2I_5$ films (0.75 μs), implying that after indium doping, the capture of excited electrons by surface states was inhibited. The efficient utilization of the excited carriers resulted in a high PLQY as well as a long lifetime. A high PLQY of 90.2% was achieved in the $Cs_3Cu_2I_5$:In films [Fig. 2(e)]. We propose that extra incorporation of In^+ brings a new radiative recombination channel and accelerates the energy transfer, improving the utilization of excitons, as well as the PLQY. The high PLQY of the scintillation films ensures a subsequent high RL light yield [44]. Figure 2(f) shows the self-trapped exciton (STE) emission mechanism of the $Cs_3Cu_2I_5$. Under the excitation of an external light source, electrons transitioned from the valence band to the conduction band, and the excited state underwent transient lattice distortion under strong electron phonon coupling, forming the STE state [47]. Due to the low STE barrier, a quantity of electrons relaxed to the STE state, ultimately combining with holes to produce bright blue emissions.

C. X-Ray Detection Performance of $Cs_3Cu_2I_5$:In Films

The high PLQY, short decay time, low preparation cost, good stability, and simple large area preparation process of the $Cs_3Cu_2I_5$:In films promise their application in large-scale

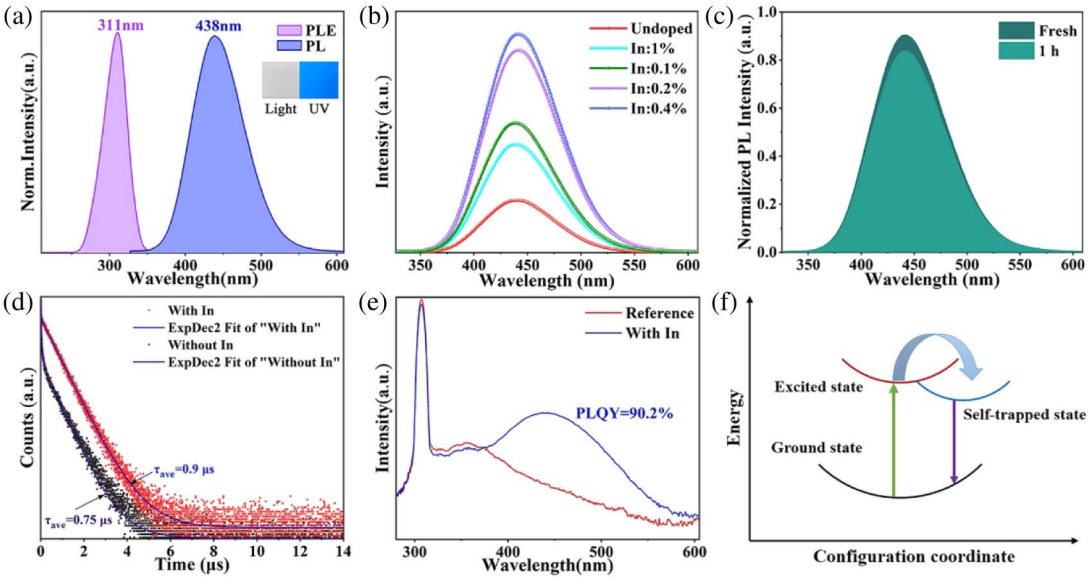

Fig. 2. Ultraviolet detection performance of the $Cs_3Cu_2I_5$:In films. (a) PL and PLE spectra of the $Cs_3Cu_2I_5$:In films. (b) PL emission spectra of the $Cs_3Cu_2I_5$ films doped with different indium concentrations. (c) Comparison of the PL spectra of the films before and after being soaked in deionized water for 1 h. (d) PL decay spectra of the $Cs_3Cu_2I_5$ films with and without In^+. (e) PLQY spectra of the $Cs_3Cu_2I_5$:In films. (f) Configuration coordinate diagram of the photophysical dynamics in $Cs_3Cu_2I_5$.

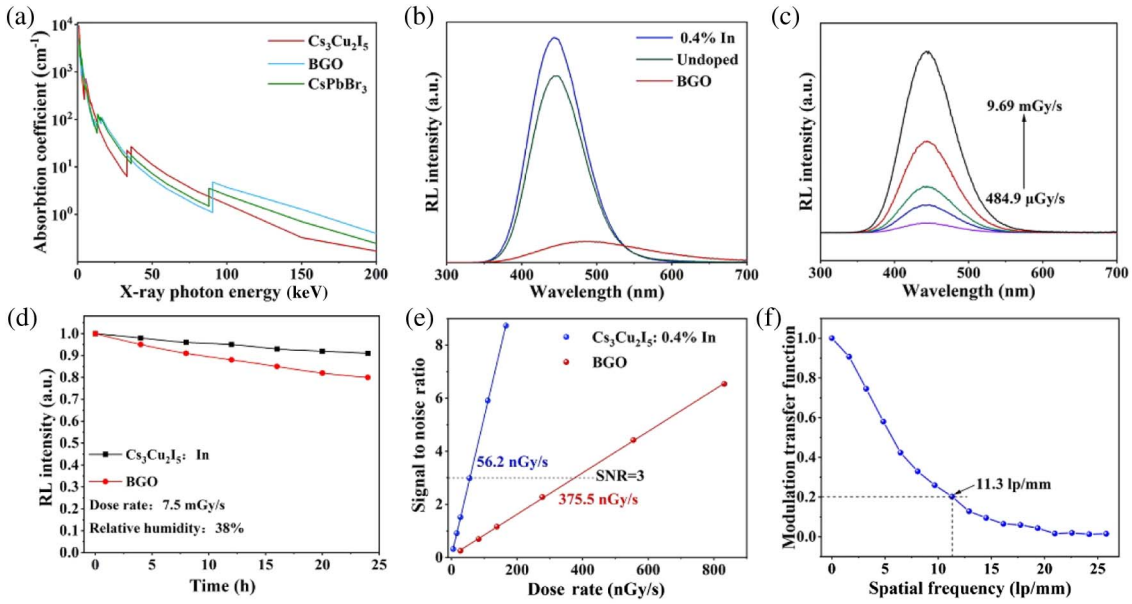

Fig. 3. X-ray detection performance of the $Cs_3Cu_2I_5$:In powders. (a) X-ray absorption coefficients of the $Cs_3Cu_2I_5$ film, the $CsPbBr_3$ film, and commercial BGO scintillator as a function of photon energy. (b) RL spectra of the $Cs_3Cu_2I_5$:0.4%In films, the undoped $Cs_3Cu_2I_5$ films, and the BGO films (dose rate, 4.85 mGy/s; voltage, 50 kV). The size (1 cm × 1 cm) and thickness (1 mm) of the films are the same. (c) Dose-rate-dependent RL spectra of the $Cs_3Cu_2I_5$:In films. (d) Normalized RL intensity of $Cs_3Cu_2I_5$:In films and BGO under 24 h continuous radiation irradiation with an X-ray dose rate of 7.5 m Gy/s. (e) Signal-to-noise ratio of X-ray response of the $Cs_3Cu_2I_5$:In films at different irradiation dose rates. (f) MTF of the $Cs_3Cu_2I_5$:In films, measured by the slanted-edge method.

practical X-ray radiography. To effectively evaluate the performance of the $Cs_3Cu_2I_5$ films, the absorption coefficients of the $Cs_3Cu_2I_5$ film, commercial BGO scintillator, and $CsPbBr_3$ film under the same conditions were recorded and compared horizontally [Fig. 3(a)]. The absorption coefficient of the $Cs_3Cu_2I_5$ film was much higher than that of the $CsPbBr_3$ film and commercial BGO scintillator from 33 to 60 keV covered by the clinical radiology area, which means that lower detection doses can be achieved in medical testing. The commercial BGO scintillator was used as a reference to estimate the light yield of the $Cs_3Cu_2I_5$ films [48] since the RL spectral range of BGO is similar to $Cs_3Cu_2I_5$. The films were fabricated to keep the same size and thickness as the BGO wafer, and RL curves were obtained using the spectrometer under an identical configuration [Fig. 3(b)]. The results showed that the $Cs_3Cu_2I_5$:0.4%In film exhibited the strongest RL response, 5.34 times higher than that of the BGO (with a light yield of 10,000 photons/MeV), and the undoped $Cs_3Cu_2I_5$ film was also 4.49 times that of the BGO. The RL strength of the $Cs_3Cu_2I_5$:In films exhibited a perfect linear relationship from 484.9 μGy/s to 9.69 mGy/s [Fig. 3(c)]. There was no significant difference between the RL spectrum and the PL spectrum, implying identical composite framework under UV irradiation and X-ray irradiation. After 24 h of irradiation with an X-ray dose rate of 7.5 mGy/s, the RL intensity could still be maintained at about 90%, while for BGO scintillators, its RL intensity decreased to 80% of its initial intensity, implying that the $Cs_3Cu_2I_5$:In films had good X-ray tolerance [Fig. 3(d)]. In addition, under a signal-to-noise ratio (SNR) of 3, the detection limit was 56.2 nGy/s [Fig. 3(e)], which was lower than that of the BGO scintillator (375.5 nGy/s) and approximately 98 times lower than the dose of the typical X-ray medical imaging (5.5 μGy/s) [49–52]. Due to its excellent scintillation performance, the $Cs_3Cu_2I_5$:In films achieved an ideal spatial resolution of 11.3 lp/mm at the MTF value of 0.2 [Fig. 3(f)], slightly higher than some recently reported X-ray scintillators [38,53,54]. Table 1 summarizes the scintillation performance of the studied $Cs_3Cu_2I_5$:In at the PDMS flexible scintillator screen and other reported scintillator materials. Compared with other copper-based perovskites and lead containing perovskites, the $Cs_3Cu_2I_5$:In films exhibited stronger relative light output, lower detection limit, and higher spatial resolution. The $Cs_3Cu_2I_5$:In films could maintain better radiation stability compared to lead perovskites. Meanwhile, the solution method is more economical and environment friendly than hot injection, cooling crystallization, evaporation method, etc.

D. Construction and Application of High-Performance X-Ray Testing System

To demonstrate the potential application of the $Cs_3Cu_2I_5$:In films in X-ray scintillation, an X-ray image system was constructed with an X-ray source, an X-ray detector, and a computer placed in sequence [Fig. 4(a)]. As a proof-of-concept experiment, the self-made system based on the $Cs_3Cu_2I_5$:In scintillator film with 220 μm thickness was used to evaluate the X-ray imaging performance. The standard resolution test sample was placed on the $Cs_3Cu_2I_5$:In films, and we observed the resolution limit of 10 lp/mm, as shown in Fig. 4(b), coinciding well with the calculated MFT result in Fig. 3(f). Through X-ray imaging systems, we could clearly see the fine

Table 1. Summary of X-Ray Scintillation Performances of Scintillators

Materials	Light Yield [photons MeV^{-1}]	Detection Limit [nGy s^{-1}]	Spatial Resolution [lp mm^{-1}]	Radiation Stability	Preparation Method	Reference
$CsPbBr_3$	21,000	–	–	2 h (unchanged)	Hot injection	[23]
$CH_3NH_3PbBr_3$	–	16	5.4	21 h (>80%)	Solution method	[55]
TPP_2MnBr_4	78,000	8.8	15.7	–	Antisolvent method	[56]
Rb_2CuBr_3	91,056	121.5	–	–	Cooling crystallization	[27]
$(C_8H_{20}N)_2MnBr_4$	24,400	24.2	4.9	250 min (>95%)	Evaporation method	[32]
K_2CuBr_3	23,806	132.8	–	–	Solution method	[30]
$CsCu_2I_3$	21,580	–	7.5	100 h (unchanged)	Cooling crystallization	[57]
$Cs_3Cu_2I_5$	46,000	96.54	8.6	–	Solution method	[54]
$Cs_3Cu_2I_5$:Zn	–	310	15.7	–	Hot injection	[42]
Cs_2ZrCl_6	49,400	65	18	120 min (>94%)	Solution method	[49]
$Cs_2Ag_{0.6}Na_{0.4}In_{1-y}Bi_yCl_6$	39,000 ± 7000	19	4.4	50 h (unchanged)	Hydrothermal method	[58]
$Cs_2Na_{0.9}Ag_{0.1}LuCl_6:Dy^{3+}$	8332	123.79	11.2	–	Hydrothermal method	[59]
$Cs_3Cu_2I_5$:In	≈53,400	56.2	11.3	24 h (>90%)	Solution method	This work

structures inside the earphone that could not be directly recognized by eyes [Fig. 4(c)]. The internal circuitry of the microchip was revealed in detail, indicating that the $Cs_3Cu_2I_5$:In films possessed immense potential for application in industrial flaw detection [Fig. 4(d)]. We also imaged the charger and could see its internal structure very clearly, further indicating the $Cs_3Cu_2I_5$:In films have great potential in imaging detection [Fig. 4(e)]. To evaluate the imaging effect on non-planar objects, we covered a pen with the $Cs_3Cu_2I_5$:In films. The spring and fill inside the pen could be clearly displayed, and there was no haloing or ghosting [Fig. 4(f)], indicating that the films also had a good imaging effect on the curved surface. This further proved that the flexible films had excellent mechanical stability and could maintain good imaging quality on non-planar

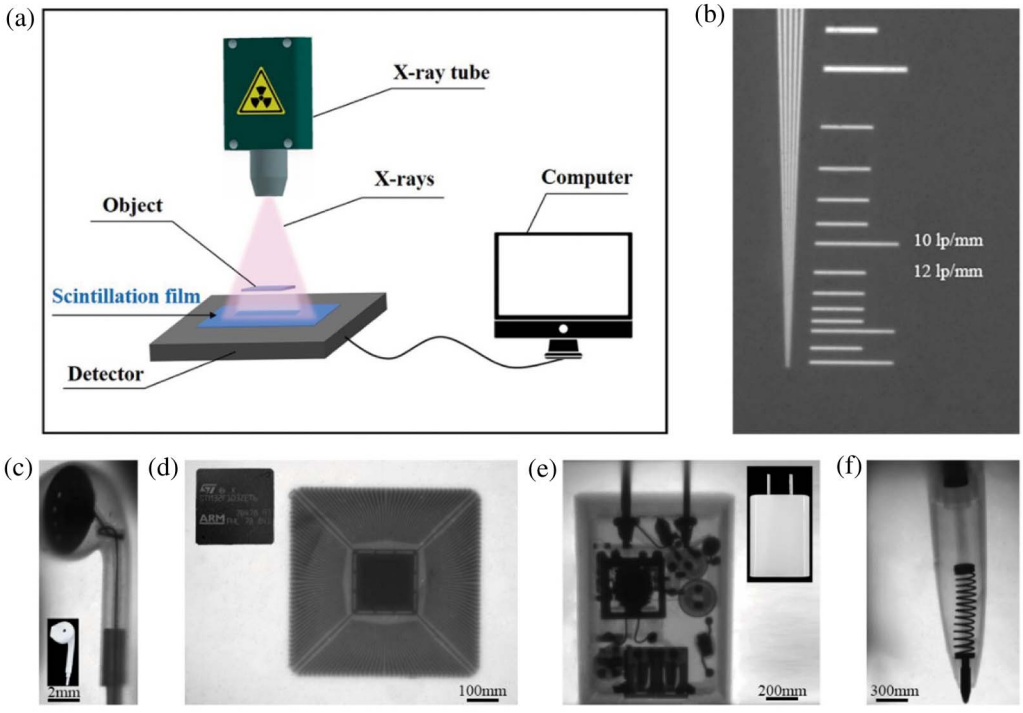

Fig. 4. Construction and application of a high-performance X-ray testing system. (a) Schematic diagram of the X-ray imaging system. (b) X-ray imaging of the $Cs_3Cu_2I_5$:In films on the standard resolution card. (c) Photograph and X-ray image (dose rate, 963 μGy/s; tube voltage, 50 kV; beam current, 200 μA; exposure time, 10 s) of internal structure of the earphone; (d) internal circuitry of the microchip; (e) internal structure of the charger plug; (f) internal spring and filling of the pen.

objects. These results demonstrated that the $Cs_3Cu_2I_5$:In films can realize X-ray imaging in complex environments.

4. CONCLUSION

In summary, we demonstrated a facile solution-synthesis route to synthesize high-performance indium-doped perovskite-related $Cs_3Cu_2I_5$ X-ray scintillator powders and a flexible scintillator film of $Cs_3Cu_2I_5$:In/PDMS at an arbitrary size for X-ray imaging. The $Cs_3Cu_2I_5$:In film exhibited bright blue light emission with a large Stokes shift of 127 nm and a high PLQY of 90.2%, and achieved good environmental stability. After continuous X-ray irradiation, soaking in deionized water, and continuous bending and stretching, the luminescence and imaging properties of the films remained stable. Benefiting from ultralow self-absorption and high PLQY, a high relative light output was obtained, more than 5 times higher than that of the BGO. The $Cs_3Cu_2I_5$:In films achieved an ultralow detection limit of 56.2 nGy/s, approximately 98 times lower than the dose of typical X-ray medical imaging. The films also exhibited outstanding X-ray imaging performance, with a high resolution of 11.3 lp/mm, excellent stability under ambient conditions, and undistorted non-planar imaging. To sum up, the presented low-cost, stable, and high-luminous-efficiency $Cs_3Cu_2I_5$:In flexible scintillator films have great application prospects in high-performance X-ray imaging.

Funding. National Natural Science Foundation of China (52275562); National Key Research and Development Program of China (2019YFB1503200).

Acknowledgment. The authors appreciate the Analytical and Testing Center and Flexible Electronics Research Center of Huazhong University of Science and Technology for the XRD and XPS measurements. The authors also acknowledge the Measurement Laboratory of Collaborative Innovation Center for Digital Intelligent Manufacturing Technology and Application for support in SEM testing.

Disclosures. The authors declare no conflicts of interest.

Data Availability. The data that support the findings of this study are available from the corresponding author upon reasonable request.

REFERENCES

1. H. Tsai, F. Liu, S. Shrestha, *et al.*, "A sensitive and robust thin-film X-ray detector using 2D layered perovskite diodes," Sci. Adv. **6**, eaay815 (2020).
2. V. B. Mykhaylyk, H. Kraus, and M. Saliba, "Bright and fast scintillation of organolead perovskite $MAPbBr_3$ at low temperatures," Mater. Horiz. **6**, 1740–1747 (2019).
3. M. Zhang, X. Wang, B. Yang, *et al.*, "Metal halide scintillators with fast and self-absorption-free defect-bound excitonic radioluminescence for dynamic X-ray imaging," Adv. Funct. Mater. **31**, 2009973 (2020).
4. S. Deumel, A. van Breemen, G. Gelinck, *et al.*, "High-sensitivity high-resolution X-ray imaging with soft-sintered metal halide perovskites," Nat. Electron. **4**, 681–688 (2021).
5. J. Zhao, L. Zhao, Y. Deng, *et al.*, "Perovskite-filled membranes for flexible and large-area direct-conversion X-ray detector arrays," Nat. Photonics **14**, 612–617 (2020).
6. M. J. Weber, "Inorganic scintillators: today and tomorrow," J. Lumin. **100**, 35–45 (2002).
7. P. Lecoq, "Development of new scintillators for medical applications," Nucl. Instrum. Methods Phys. Res. A **809**, 130–139 (2016).
8. L. Borgese, F. Bilo, R. Dalipi, *et al.*, "Total reflection X-ray fluorescence as a tool for food screening," Spectrochim. Acta B **113**, 1–15 (2015).
9. F. Maddalena, L. Tjahjana, A. Xie, *et al.*, "Inorganic, organic, and perovskite halides with nanotechnology for high-light yield X- and γ-ray scintillators," Crystals **9**, 88 (2019).
10. K. Naresh, K. A. Khan, R. Umer, *et al.*, "The use of X-ray computed tomography for design and process modeling of aerospace composites: a review," Mater. Des. **190**, 108553 (2020).
11. J. A. Rowlands, "Material change for X-ray detectors," Nature **550**, 47–48 (2017).
12. H. Wei and J. Huang, "Halide lead perovskites for ionizing radiation detection," Nat. Commun. **10**, 1066 (2019).
13. T. Chen, X. Li, Y. Wang, *et al.*, "Centimeter-sized $Cs_3Cu_2I_5$ single crystals grown by oleic acid assisted inverse temperature crystallization strategy and their films for high-quality X-ray imaging," J. Energy Chem. **79**, 382–389 (2023).
14. J. H. Heo, D. H. Shin, J. K. Park, *et al.*, "High-performance next-generation perovskite nanocrystal scintillator for nondestructive X-ray imaging," Adv. Mater. **30**, 1801743 (2018).
15. W. Mengesha, T. D. Taulbee, B. D. Rooney, *et al.*, "Light yield nonproportionality of CsI (Tl), CsI (Na), and YAP," IEEE Trans. Nucl. Sci. **45**, 456–461 (1998).
16. I. Mouhti, A. Elanique, M. Y. Messous, *et al.*, "Characterization of CsI (Tl) and LYSO (Ce) scintillator detectors by measurements and Monte Carlo simulations," Appl. Radiat. Isot. **154**, 108878 (2019).
17. A. Kryemadhi, L. Barner, A. Grove, *et al.*, "A LYSO crystal array readout by silicon photomultipliers as compact detector for space applications," Nucl. Instrum. Methods Phys. Res. A **912**, 93–96 (2018).
18. S. Weber, D. Christ, M. Kurzeja, *et al.*, "Comparison of LuYAP, LSO, and BGO as scintillators for high resolution PET detectors," IEEE Trans. Nucl. Sci. **50**, 1370–1372 (2003).
19. E. V. D. van Loef, P. Dorenbos, C. W. E. van Eijk, *et al.*, "High-energy-resolution scintillator: Ce^{3+} activated $LaBr_3$," Appl. Phys. Lett. **79**, 1573–1575 (2001).
20. C. W. E. van Eijk, "Inorganic scintillators in medical imaging," Phys. Med. Biol. **47**, R85–R106 (2002).
21. O. Moseley, T. Doherty, R. Parmee, *et al.*, "Halide perovskites scintillators: unique promise and current limitations," J. Mater. Chem. C **9**, 11588–11604 (2021).
22. A. Y. Martin Nikl, "Recent R&D trends in inorganic single-crystal scintillator materials for radiation detection," Adv. Opt. Mater. **3**, 463–481 (2015).
23. Y. Zhang, R. Sun, X. Ou, *et al.*, "Metal halide perovskite nanosheet for X-ray high-resolution scintillation imaging screens," ACS Nano **13**, 2520–2525 (2019).
24. Y. Cao, J. Wei, C. Li, *et al.*, "Optimal operating control strategy for biogas generation under electricity spot market," J. Eng. **2019**, 5183–5186 (2019).
25. Y. Li, P. Vashishtha, Z. Zhou, *et al.*, "Room temperature synthesis of stable, printable $Cs_3Cu_2X_5$ (X = I, Br/I, Br, Br/Cl, Cl) colloidal nanocrystals with near-unity quantum yield green emitters (X = Cl)," Chem. Mater. **32**, 5515–5524 (2020).
26. Q. Chen, J. Wu, X. Ou, *et al.*, "All-inorganic perovskite nanocrystal scintillators," Nature **561**, 88–93 (2018).
27. B. Yang, L. Yin, G. Niu, *et al.*, "Lead-free halide Rb_2CuBr_3 as sensitive X-ray scintillator," Adv. Mater. **31**, 1904711 (2019).
28. S. Seth, T. Ahmed, A. De, *et al.*, "Tackling the defects, stability, and photoluminescence of $CsPbX_3$ perovskite nanocrystals," ACS Energy Lett. **4**, 1610–1618 (2019).
29. Q. Zhou, J. Ren, J. Xiao, *et al.*, "Highly efficient copper halide scintillators for high-performance and dynamic X-ray imaging," Nanoscale **13**, 19894–19902 (2021).
30. W. Gao, G. Niu, L. Yin, *et al.*, "One-dimensional all-inorganic K_2CuBr_3 with violet emission as efficient X-ray scintillators," ACS Appl. Electron. Mater. **2**, 2242–2249 (2020).

31. Y. Zhou, X. Wang, T. He, *et al.*, "Large-area perovskite-related copper halide film for high-resolution flexible X-ray imaging scintillation screens," ACS Energy Lett. **7**, 844–846 (2022).
32. T. Jiang, W. Ma, H. Zhang, *et al.*, "Highly efficient and tunable emission of lead-free manganese halides toward white light-emitting diode and X-ray scintillation applications," Adv. Funct. Mater. **31**, 2009973 (2021).
33. T. Jun, T. Handa, K. Sim, *et al.*, "One-step solution synthesis of white-light-emitting films via dimensionality control of the Cs-Cu-I system," Appl. Mater. **7**, 111113 (2019).
34. P. Cheng, L. Sun, L. Feng, *et al.*, "Colloidal synthesis and optical properties of all-inorganic low-dimensional cesium copper halide nanocrystals," Angew. Chem. Int. Ed. **58**, 16087–16091 (2019).
35. Y. Li, Z. Shi, W. Liang, *et al.*, "Highly stable and spectrum-selective ultraviolet photodetectors based on lead-free copper-based perovskites," Mater. Horiz. **7**, 530–540 (2020).
36. W. Liang, L. Wang, Y. Li, *et al.*, "Stable and ultraviolet-enhanced broadband photodetectors based on Si nanowire arrays-$Cs_3Cu_2I_5$ nanocrystals hybrid structures," Mater. Today Phys. **18**, 100398 (2021).
37. S. Cheng, A. Beitlerova, R. Kucerkova, *et al.*, "Zero-dimensional $Cs_3Cu_2I_5$ perovskite single crystal as sensitive X-ray and γ-ray scintillator," Phys. Status Solidi-RRL **14**, 2000374 (2020).
38. N. Li, Z. Xu, Y. Xiao, *et al.*, "Flexible, high scintillation yield $Cs_3Cu_2I_5$ film made of ball-milled powder for high spatial resolution X-ray imaging," Adv. Opt. Mater. **10**, 2102232 (2022).
39. Z. Guo, J. Li, R. Pan, *et al.*, "All-inorganic copper(I)-based ternary metal halides: promising materials toward optoelectronics," Nanoscale **12**, 15560–15576 (2020).
40. D. Yuan, "Air-stable bulk halide single-crystal scintillator $Cs_3Cu_2I_5$ by melt growth: intrinsic and Tl doped with high light yield," ACS Appl. Mater. Interfaces **12**, 38333–38340 (2020).
41. X. Li, J. Chen, D. Yang, *et al.*, "Mn^{2+} induced significant improvement and robust stability of radioluminescence in $Cs_3Cu_2I_5$ for high-performance nuclear battery," Nat. Commun. **12**, 3879 (2021).
42. K. Qu, Y. Lu, P. Ran, *et al.*, "Zn (II)-doped cesium copper halide nanocrystals with high quantum yield and colloidal stability for high-resolution X-ray imaging," Adv. Opt. Mater. **11**, 2202883 (2023).
43. Q. Wang, Q. Zhou, M. Nikl, *et al.*, "Highly resolved X-ray imaging enabled by In(I) doped perovskite-like $Cs_3Cu_2I_5$ single crystal scintillator," Adv. Opt. Mater. **10**, 2200304 (2022).
44. X. Hu, P. Yan, P. Ran, *et al.*, "*In situ* fabrication of $Cs_3Cu_2I_5$: Tl nanocrystal films for high-resolution and ultrastable X-ray imaging," J. Phys. Chem. Lett. **13**, 2862–2870 (2022).
45. T. Jun, K. Sim, S. Iimura, *et al.*, "Lead-free highly efficient blue-emitting $Cs_3Cu_2I_5$ with 0D electronic structure," Adv. Mater. **30**, 1804547 (2018).
46. H. Peng, Y. Tian, Z. Zhang, *et al.*, "Bulk assembly of zero-dimensional organic copper bromide hybrid with bright self-trapped exciton emission and high antiwater stability," J. Phys. Chem. C **125**, 20014–20021 (2021).
47. T. Hu, M. D. Smith, E. R. Dohner, *et al.*, "Mechanism for broadband white-light emission from two-dimensional (110) hybrid perovskites," J. Phys. Chem. Lett. **7**, 2258–2263 (2016).
48. T. He, Y. Zhou, X. Wang, *et al.*, "High-performance copper-doped perovskite-related silver halide X-ray imaging scintillator," ACS Energy Lett. **7**, 2753–2760 (2022).
49. F. Zhang, Y. Zhou, Z. Chen, *et al.*, "Thermally activated delayed fluorescence zirconium-based perovskites for large-area and ultraflexible X-ray scintillator screens," Adv. Mater. **34**, 2204801 (2022).
50. Z. Li, F. Zhou, H. Yao, *et al.*, "Halide perovskites for high-performance X-ray detector," Mater. Today **48**, 155–175 (2021).
51. Y. Haruta, M. Kawakami, Y. Nakano, *et al.*, "Scalable fabrication of metal halide perovskites for direct X-ray flat-panel detectors: a perspective," Chem. Mater. **34**, 5323–5333 (2022).
52. H. Wu, Y. Ge, G. Niu, *et al.*, "Metal halide perovskites for X-ray detection and imaging," Matter **4**, 144–163 (2021).
53. R. Duan, Z. Chen, D. Xiang, *et al.*, "Large-area flexible scintillator screen based on copper-based halides for sensitive and stable X-ray imaging," J. Lumin. **253**, 119482 (2023).
54. X. Zhao, T. Jin, W. Gao, *et al.*, "Embedding $Cs_3Cu_2I_5$ scintillators into anodic aluminum oxide matrix for high-resolution X-ray imaging," Adv. Opt. Mater. **9**, 2101194 (2021).
55. Q. Xu, S. Zhou, J. Huang, *et al.*, "Ultra-flexible and highly sensitive scintillation screen based on perovskite quantum dots for non-flat objects X-ray imaging," Mater. Today Phys. **18**, 100390 (2021).
56. K. Han, K. Sakhatskyi, J. Jin, *et al.*, "Seed-crystal-induced cold sintering toward metal halide transparent ceramic scintillators," Adv. Mater. **34**, 2110420 (2022).
57. M. Zhang, J. Zhu, B. Yang, *et al.*, "Oriented-structured $CsCu_2I_3$ film by close-space sublimation and nanoscale seed screening for high-resolution X-ray imaging," Nano Lett. **21**, 1392–1399 (2021).
58. W. Zhu, W. Ma, Y. Su, *et al.*, "Low-dose real-time X-ray imaging with nontoxic double perovskite scintillators," Light Sci. Appl. **9**, 112 (2020).
59. N. Zhang, R. Zhang, X. Xu, *et al.*, "X-ray-activated long afterglow double-perovskite scintillator for detection and extension imaging," Adv. Opt. Mater. **11**, 2300187 (2023).